PHYSICAL REVIEW C **82**, 054909 (2010)

Thermal photons from heavy ion collisions: A spectral function approach

Kevin Dusling[1] and Ismail Zahed[2]
[1]*Physics Department, Building 510A, Brookhaven National Laboratory, Upton, New York 11973, USA*
[2]*Department of Physics and Astronomy, State University of New York, Stony Brook, New York 11794, USA*

(Received 20 April 2010; published 29 November 2010)

We analyze the photon rates from a hadronic gas in equilibrium using chiral-reduction formulas and a density expansion. The chiral reduction is carried to second order in the pion density, which in principal includes all kinetic processes of the type $X \to \pi\gamma$ and $X \to \pi\pi\gamma$. The resulting rates are encoded in the form of vacuum correlation functions, which are amenable to experiment. The hadronic rates computed in this work along with the known perturbative quark gluon plasma rates are integrated over the space-time evolution of a hydrodynamic model tuned to hadronic observables. The resulting yields are compared to the recent photon and low-mass dilepton measurements at the Super Proton Synchrotron and Relativistic Heavy Ion Collider. Predictions for the Large Hadron Collider are made.

DOI: 10.1103/PhysRevC.82.054909 PACS number(s): 25.75.Cj

I. INTRODUCTION

Electromagnetic emissions in ultrarelativistic collisions are thermally dominated in the low to intermediate mass (M) and q_T regions. Thermalization at the Relativistic Heavy Ion Collider (RHIC) was established from detailed flow measurements of hadrons. PHENIX observed a large dielectron emission in the mass region below the ρ ($M \approx 770$ MeV). These emissions are much larger than those reached theoretically. The dielectron excess reported by PHENIX is one of the most dramatic pieces of data stemming from RHIC.

The PHENIX collaboration also recently reported on photon spectra in the intermediate-q_T region. There is one caveat, in that PHENIX did not actually measure real photons but low-mass dielectron spectra, which were then extrapolated to the photon point. In this case, their finding was an excess of photons at intermediate q_T ($1 \leqslant q_T \lesssim 2.5$ GeV) momentum. In this case the excess was in line with that reached theoretically.

Our qualitative summary of the preceding two PHENIX measurements is as follows. PHENIX observed an excess of dielectron pairs at low mass. This excess is consistent with theoretical expectations at intermediate q_T ($1 \leqslant q_T \lesssim 2.5$ GeV) momentum. The excess seen at low momentum, $q_T \lesssim 1$ GeV, is well above any theoretical calculations made to date.

Thermal emissions at low to intermediate invariant mass (M) and q_T are involved due to the many reaction processes involving hadrons and the strong character of their interactions. The only organizational principles are broken chiral symmetry and gauge invariance, both of which are difficult to assert in reaction processes with hadrons in general. If hadrons thermalize with the pions and nucleons as the only strongly stable constituents, then there is a way to systematically organize the electromagnetic emissivities by expanding them, not in terms of processes but rather in terms of final hadronic states. The emissivities are then amenable to spectral functions by chiral reduction. These spectral functions are either tractable from other experiments or amenable to resonance saturation.

In Sec. II, we derive the photon emission rates from a thermal hadronic environment in terms of one- and two-pion final states. We use the chiral-reduction formulas to rewrite the rates in terms of spectral functions. In Secs. II A and II B, we compare our rates to some key processes based on kinetic theory as well as the leading-order quark gluon plasma (QGP) rates. In Sec. II C we comment on the experimental extrapolation procedure used recently by RHIC to measure the photon emissivities by extrapolating the dilepton rates to the photon point.

The remaining part of this work consists of comparison with experimental data, which is performed by integrating the rates over the space-time evolution of a hydrodynamic simulation described in Sec. III. Sections III A, III B, and III C show our findings for WA98 and PHENIX. Section III D contains our predictions for the Large Hadron Collider (LHC).

II. HADRONIC PHOTON RATES

For a hadronic gas in thermal equilibrium, the number of photons produced per unit four-volume and unit three-momentum can be related to the electromagnetic current-current correlation function [1]

$$q^0 \frac{dN}{d^3q} = -\frac{\alpha_{\rm em}}{4\pi^2}\mathbf{W}(q), \tag{1}$$

with $q^2 = 0$ and

$$\mathbf{W}(q) = \int d^4x\, e^{-iqx}\,\mathrm{Tr}[e^{-(\mathbf{H}-F)/T}\mathbf{J}^\mu(x)\mathbf{J}_\mu(0)]. \tag{2}$$

In the preceding expression, $\mathbf{J}_\mu$ is the hadronic part of the electromagnetic current, $\mathbf{H}$ is the hadronic Hamiltonian, and F is the free energy. Below the phase transition, the trace is carried over stable states with respect to the strong interaction (e.g., pions and nucleons). From the spectral representation and symmetry we can re-express the correlator in terms of the absorptive part of the time-ordered correlation function

$$\mathbf{W}(q) = \frac{2}{1+e^{q^0/T}}\,\mathrm{Im}\,\mathbf{W}^F(q), \tag{3}$$

where

$$\mathbf{W}^F(q) = i\int d^4x e^{iqx}\,\mathrm{Tr}[e^{-(\mathbf{H}-F)/T}\mathcal{T}\mathbf{J}^\mu(x)\mathbf{J}_\mu(0)]. \tag{4}$$

In this work, we consider a heat bath that is nucleon free. In this case the trace can be expanded as

$$\mathbf{W}^F(q) = \mathbf{W}_0 + \int d\pi_1 \mathbf{W}_\pi + \frac{1}{2!}\int d\pi_1 d\pi_2 \mathbf{W}_{\pi\pi} + \cdots, \tag{5}$$

where $d\pi_i$ are the pion phase-space factors given by

$$d\pi_i = \frac{d^3k_i}{(2\pi)^3}\frac{n(E_i)}{2E_i}. \tag{6}$$

In the preceding density expansion, we defined

$$\begin{aligned} \mathbf{W}_0 &= i\int d^4x e^{iqx}\langle 0|\mathcal{T}\mathbf{J}^\mu(x)\mathbf{J}_\mu(0)|0\rangle, \\ \mathbf{W}_\pi &= i\int d^4x e^{iqx}\langle \pi^a(k_1)|\mathcal{T}\mathbf{J}^\mu(x)\mathbf{J}_\mu(0)|\pi^a(k_1)\rangle, \\ \mathbf{W}_{\pi\pi} &= i\int d^4x e^{iqx}\langle \pi^a(k_1)\pi^b(k_2)|\mathcal{T} \\ &\quad \times \mathbf{J}^\mu(x)\mathbf{J}_\mu(0)|\pi^a(k_1)\pi^b(k_2)\rangle, \end{aligned} \tag{7}$$

where the indices a and b are summed over isospin. These are the first three terms in an expansion in terms of the pion density.[1]

The first contribution in Eqs. (7) is dominated by the transverse part of the isovector correlator and is fixed entirely by the measured electroproduction data. It vanishes for real photons because the heat bath is stable against spontaneous photon emission.[2] Therefore, $\mathbf{W}_0 = 0$ and does not contribute to the photon emissivities. The next two terms, $\mathbf{W}_\pi$ and $\mathbf{W}_{\pi\pi}$, can be reduced to measurable vacuum correlators by the chiral reduction formulas [2]. The one-pion reduced contribution $\mathbf{W}_\pi$ is now standard. Its dominant contribution involves VV and AA correlators in the vacuum, and reads [3]

$$\begin{aligned} \mathbf{W}_\pi^F(q,k) &= \frac{12}{f_\pi^2}q^2 \mathrm{Im}\,\mathbf{\Pi}_V(q^2) - \frac{6}{f_\pi^2}(k+q)^2 \mathrm{Im}\,\mathbf{\Pi}_A[(k+q)^2] \\ &\quad + (q \to -q) + \frac{8}{f_\pi^2}\left[(kq)^2 - m_\pi^2 q^2\right]\mathrm{Im}\,\mathbf{\Pi}_V(q^2) \\ &\quad \times \mathrm{Re}\,\Delta_R(k+q) + (q \to -q), \end{aligned} \tag{8}$$

where $\mathrm{Re}\,\Delta_R$ is the real part of the retarded pion propagator, and $\mathbf{\Pi}_V$ and $\mathbf{\Pi}_A$ are the transverse parts of the VV and AA correlators. Their spectral functions are related to both e^+e^- annihilation and τ-decay data, as was compiled in Ref. [4].

The two-pion reduced contribution $\mathbf{W}_{\pi\pi}$ is more involved. Its full unwinding can be found in Ref. [5]. We quote only the dominant contributions:

$$\begin{aligned} &\frac{1}{f_\pi^4}W_{\pi\pi}^F(q,k_1,k_2) \\ &= \frac{2}{f_\pi^2}[g_{\mu\nu} - (2k_1+q)_\mu k_{1\nu}\mathrm{Re}\,\Delta_R(k_1+q)]\mathrm{Im}\,\mathcal{T}_{\pi\gamma}^{\mu\nu}(q,k_2) \\ &\quad + (q \to -q) + (k_1 \to -k_1) + (q, k_1 \to -q, -k_1) \\ &\quad + \frac{1}{f_\pi^2}k_1^\mu(2k_1+q)^\nu \mathrm{Re}\,\Delta_R(k_1+q)\epsilon^{a3e}\epsilon^{e3g}\mathrm{Im}\,\mathcal{B}_{\mu\nu}^{ag}(k_1,k_2) \\ &\quad - \frac{1}{f_\pi^2}[g^{\mu\nu} - (k_1+q)^\mu(2k_1+q)^\nu \mathrm{Re}\,\Delta_R(k_1+q)] \\ &\quad \times \epsilon^{a3e}\epsilon^{a3f}\mathrm{Im}\,\mathcal{B}_{\mu\nu}^{ef}(k_1+q,k_2) \\ &\quad + \frac{1}{f_\pi^2}(k_1+q)^\mu(k_1+q)^\nu(2k_1+q)^2[\mathrm{Re}\,\Delta_R(k_1+q)]^2 \\ &\quad \times \epsilon^{a3e}\epsilon^{a3f}\mathrm{Im}\,\mathcal{B}_{\mu\nu}^{ef}(k_1+q,k_2) + (k_1 \to -k_1). \end{aligned} \tag{9}$$

The first term contains the pion-spin-averaged $\pi\gamma$ forward scattering amplitude ($\mathrm{Im}\,\mathcal{T}_{\pi\gamma}^{\mu\nu}$). For real photons ($q^2 = 0$), this is entirely constrained by photon fusion data by crossing symmetry [6], whereas for virtual photons it can be worked out by further chiral reduction as was carried out in Ref. [2]. The remaining terms all contain the contribution labeled $\mathcal{B}$, which reads

$$\begin{aligned} &\mathcal{B}_{\mu\nu}^{ef}(k_1,k_2) \\ &\quad \equiv i\int d^4x e^{ik_1x}\left\langle \pi_{\mathrm{out}}^b(k_2)\middle|\mathcal{T}\left[\mathbf{j}_{A\mu}^e(x)\mathbf{j}_{A\nu}^f(0)\right]\middle|\pi_{\mathrm{in}}^b(k_2)\right\rangle \end{aligned} \tag{10}$$

and is still amenable to further chiral reduction. The dominant contribution arises from the schematic diagrams shown in Fig. 1 resulting in the following spectral contributions:

$$\begin{aligned} \mathrm{Im}\,\mathcal{B}_{\mu\nu}^{ef}(k_1,k_2) &= \frac{2}{f_\pi^2}\delta^{ef}[g_{\mu\nu}(k_1+k_2)^2 \\ &\quad - (k_1+k_2)_\mu(k_1+k_2)_\nu]\mathrm{Im}\,\Pi_V[(k_1+k_2)^2] \\ &\quad + (k_2 \to -k_2) - \frac{4}{f_\pi^2}\delta^{ef} \\ &\quad \times \left[g_{\mu\nu}k_1^2 - k_{1\mu}k_{1\nu}\right]\mathrm{Im}\,\Pi_A\left(k_1^2\right). \end{aligned} \tag{11}$$

It is also instructive to look at the preceding results in the limit where the incoming pions are soft ($k_1, k_2 \to 0$). We then find the simple result that

$$\frac{1}{f_\pi^4}\mathbf{W}_{\pi\pi}^F(q) = \frac{16}{f_\pi^4}[\mathrm{Im}\,\Pi_A(q^2) - \mathrm{Im}\,\Pi_V(q^2)], \tag{12}$$

which reproduces the result of Eletsky and Ioffe [7]. We should also mention on a more practical level that the dominant contribution to the preceding expression comes from terms containing Π_V and one can therefore neglect terms in Eq. (2) containing $\mathcal{T}_{\pi\gamma}$ or Π_A. The dominant mechanism is therefore the first diagram on the right-hand side of Fig. 1. This corresponds to the matrix element for $\pi\pi$ scattering via exchange of a vector meson. The additional terms in Eq. (2) attach a photon to one of the external lines.

In Fig. 2 we show the photon rates stemming from $\mathbf{W}_\pi$ and $\mathbf{W}_{\pi\pi}$ for three temperatures. Clearly the two-pion emission rates provide substantial enhancement when the emitted photon is soft owing to pion bremsstrahlung. At the highest temperatures, $\mathbf{W}_{\pi\pi}$ provides an enhancement even for high-energy photons. But at these temperatures the virial expansion is clearly beyond its limit of applicability. We stress that the hadronic contributions to $\mathbf{W}_{\pi\pi}$ involve all hadronic processes in the heat bath with two pions and a photon in the final state.

---

[1] More specifically, the dimensionless expansion parameter is $\kappa \approx n_\pi/(2m_\pi f_\pi^2)$, where n_π is the pion density. This corresponds to $\kappa \approx$ 0.18, 0.30, and 0.84 at temperatures of 120, 140, and 190 MeV, respectively. We therefore expect the expansion to be reasonable unless new thresholds open up.

[2] It also vanishes for massive photons having $M \leqslant 2m_\pi$.

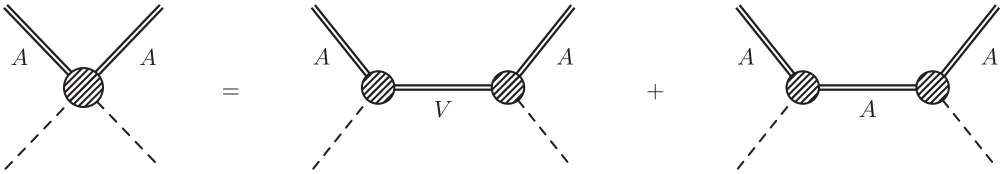

FIG. 1. Pictorial chiral reduction of $\mathcal{B}$.

A. Comparison to kinetic theory

One of the nice features of the preceding spectral-function approach is that one does not need to organize the calculation in terms of the many possible reaction mechanisms, because there is no a priori small expansion parameter in the strongly coupled hadronic phase. Instead, the calculation is organized in a virial-like expansion and all possible reaction channels should be included via the zero-temperature spectral densities. The drawback is that we lose some physical intuition as we tend to discuss photon production from a kinetic theory approach. In this section, we now compare our results with kinetic theory results performed by a number of other groups.

First let us start with our $\mathbf{W}_\pi$ piece, which was originally worked out in Ref. [3] for both dileptons and photons. From a kinetic theory standpoint, this approach should include all reactions that contain one pion in the final state. An example of the dominant contribution in this channel is $\pi\rho \to \pi\gamma$. In Fig. 3 we show the one-pion piece $\mathbf{W}_\pi$ as well as the rates stemming from the reaction $\pi\rho \to \pi\gamma$ computed in Ref. [8]. On a qualitative level, we find very good agreement, considering the rates were derived from two very different approaches. We should mention that a full SU(3) calculation [9] also includes reactions containing K and K^* (e.g., $\pi K^* \to K\gamma$).

We now come to the $\mathbf{W}_{\pi\pi}$ piece, which is new to this work. From a kinetic theory standpoint this should be identified as including all reactions with two pions in the final state and in principal can contain any number of initial-state particles. We expect the reactions $\pi\pi \to \rho\gamma$ and $\rho \to \pi\pi\gamma$ to dominate. These reactions were calculated in Ref. [8] and are shown in Fig. 3. These two kinetic processes alone cannot explain the observed enhancement that we find in our $\mathbf{W}_{\pi\pi}$ contribution. Our computed $\mathbf{W}_{\pi\pi}$ should also contain $2 \to 3$ processes such as $\pi\pi \to \pi\pi\gamma$. This reaction was worked out beyond the soft photon approximation in Ref. [10]. We show a parametrization of their results in the region $0.1 < q_0 < 0.5$ GeV in Fig. 3. On a qualitative level, we see that the pion bremsstrahlung agrees with our $\mathbf{W}_{\pi\pi}$ contribution.

We do not claim that the rates encoded in $\mathbf{W}_\pi$ and $\mathbf{W}_{\pi\pi}$ are the end of the story. In the preceding comparison, we selected the reaction channels that we expect to be implicitly included in our analysis. We can conclude that we have a good handle on many of the kinetic theory processes shown above, the most significant being the $\pi\pi$ bremsstrahling encoded in $\mathbf{W}_{\pi\pi}$. There are other reactions (e.g., $\omega \to \pi\gamma$) that, although not included in our SU(2) analysis, were shown to have strength at low energy [8,11].

B. Comparison to QGP emission

There has been great progress in the calculation of the QGP photon rates in perturbative quantum chromodynamics. We do not give the full history of these results but instead highlight some key points because they may become relevant from a phenomenological perspective.

First, the Born contribution corresponding to $q\bar{q} \to \gamma$ contributes at order α_s^0 for dileptons but vanishes at the photon point because of energy momentum conservation. Therefore, for photons, the first nontrivial contribution comes from one-loop diagrams, $O(g^2)$, corresponding to the

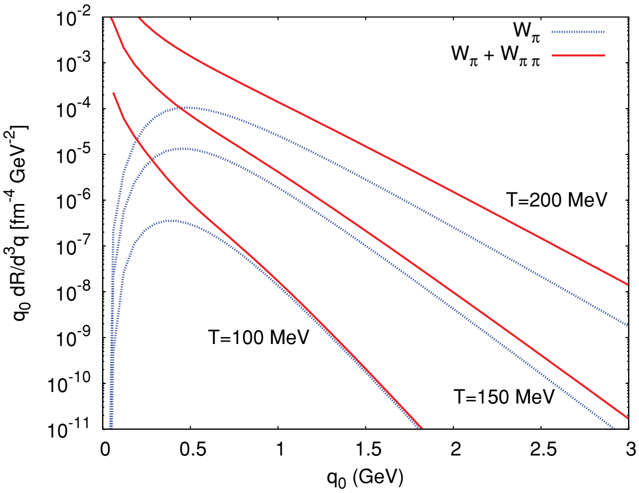

FIG. 2. (Color online) Photon emission rates $\mathbf{W}_\pi$ and $\mathbf{W}_{\pi\pi}$ for $T = 100$, 150, and 200 MeV.

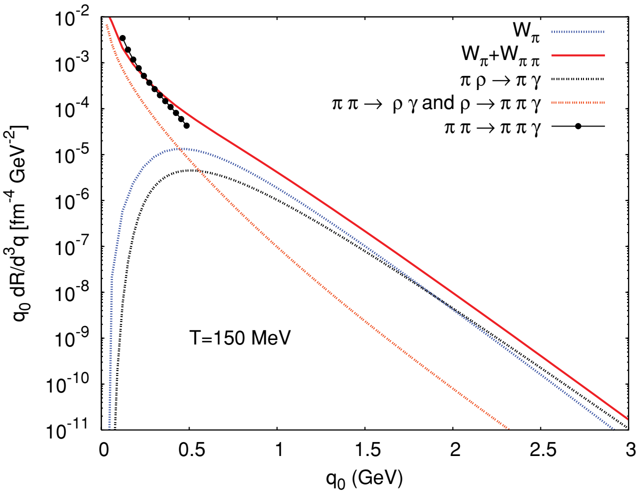

FIG. 3. (Color online) Photon rates from spectral functions vs kinetic rates. See text for details.

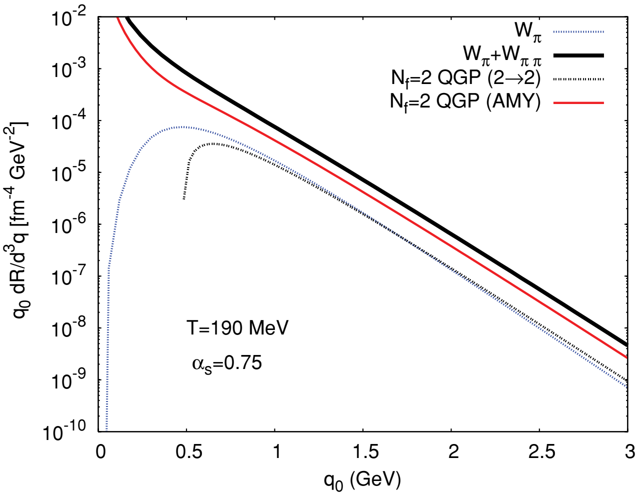

FIG. 4. (Color online) Hadronic rates from the spectral-function approach vs the perturbative QGP rates.

annihilation ($q+\overline{q} \to g\gamma$) and Compton ($g+q(\overline{q}) \to q(\overline{q})+\gamma$) processes. These diagrams contain a logarithmic singularity stemming from the exchange of a soft massless quark. The singularity is cured by including hard thermal loop (HTL) [12] corrections to the quark propagator. The net result is to give the exchanged quark a thermal mass of order gT and the rates are indeed finite, as shown in Refs. [11,13]. We plotted the photon rate owing to a $2 \to 2$ process in Fig. 4.

It was later realized in Refs. [14–16] that the $2 \to 2$ processes of annihilation and Compton scattering are not the only diagrams that contribute at order g^2. It was found that there are a class of diagrams that, even though they are naively of higher order, are promoted to order g^2 due to collinear singularities. Two examples of such processes are bremsstrahling ($qx \to \gamma qx$) and annihilation with scattering ($q\overline{q}x \to \gamma gx$), where x can be a quark, an antiquark, or a gluon.

To obtain the leading-order result, one must resum an infinite set of ladder diagrams which contribute at the same order. In resumming this infinite set of diagrams, one must also take into account the Landau-Pomeranchuk-Migdal (LPM) effect, which suppresses the rate owing to the effects of multiple collisions on the photon production process. This was demonstrated and evaluated in full in Refs. [17–19]. In this work, we use the complete leading-order rates, including the LPM effect as parametrized in Ref. [18]. The additional processes included in the full leading-order calculation give a large enhancement to the rates, as seen in Fig. 4.

The leading-order QGP rates have one parameter, α_s, which should be evaluated at a scale on the order of the temperature. In this work, we evaluate the coupling constant using the two-loop β function in an $\overline{MS}$ scheme. To assess the uncertainty in the scale choice, we evaluated the yields assuming the coupling runs with two different scales: $\mu = \pi T$ and $\mu = 2\pi T$. At $T = 400$ MeV, which is a typical initial temperature in our hydrodynamic evolution, we have $\alpha_s(\pi T) = 0.38$ versus $\alpha_s(2\pi T) = 0.26$, whereas at our chosen transition temperature of $T = 190$ MeV we have $\alpha_s(\pi T) = 0.75$ versus $\alpha_s(2\pi T) = 0.40$.

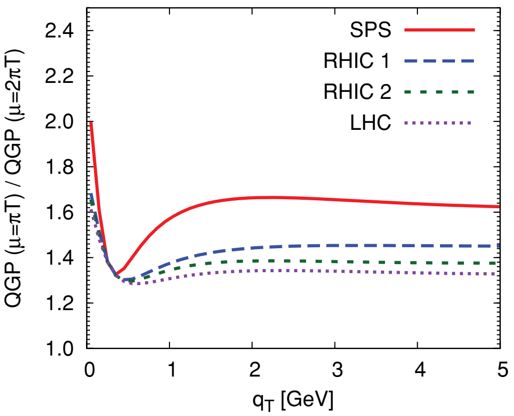

FIG. 5. (Color online) Scale dependence of the perturbative QGP yields at SPS, RHIC, and the LHC.

Even though we have yet to discuss the details of the space-time evolution (see Sec. III), it is still instructive at this point to compare the yields from the QGP phase for various systems to see the uncertainty in the scale choice. In Fig. 5 we show the ratio of the QGP yield coming from collisions at Super Proton Synchrotron (SPS), RHIC, and the LHC at the two scale choices. We focus on the results above $q_\perp \approx 1$ GeV because the perturbative rate calculations break down below this scale, as we discuss in a moment. In general, we find an enhancement in the yields by a factor of ≈60% at the SPS and ≈30% at the LHC by decreasing the scale from $2\pi T$ to πT. At the LHC there is a smaller uncertainty in the scale choice because the temperatures in the system are much higher, yielding smaller running coupling effects. This analysis shows that at RHIC there is a systematic uncertainty in the yields on the order of ≈40% owing to the scale choice. With this in mind, we have chosen to fix the scale to $\mu = \pi T$ for the remainder of this work to get an upper bound on the photon emissivities from the QGP phase.

Let us now come to Fig. 4, where we compared the hadronic and QGP rates for a broad range of photon energies. We generated the plot at the transition temperature $T = 190$ MeV, where both rates have the largest theoretical uncertainties. The QGP rates are plotted with a substantial coupling $\alpha_s = 0.75$, which is the highest value reached in the simulation. We should stress that in the transition region one should be extremely skeptical of the rates. For both the hadronic gas and the QGP, the expansion parameters have become of order 1 ($\kappa \sim 0.8$ and $g \sim 3$). One might argue that the QGP rates can be trusted as long as the argument under the log is larger than 1. This is the case as long as one remains above $q_0 \sim 1$ GeV. It is reassuring to see that the photon rates are in qualitative agreement (within a factor ≈2) as one approaches the transition region from above or below.

C. Photons versus low-mass dileptons

In this section we discuss some general considerations between photons and low-mass dileptons as well as the rates for the latter. The discussion of this section is relevant for understanding the systematic uncertainty in the recent photon measurements at PHENIX as well as understanding part of the source of the low-mass dielectron excess observed at PHENIX. We withhold the model comparison to data until Sec. III C.

The rate of dilepton production per unit four-volume and four-momentum is given by

$$\frac{dR}{d^4q} = \frac{-\alpha^2}{3\pi^3 q^2}\left(1+\frac{2m_l^2}{q^2}\right)\left(1-\frac{4m_l^2}{q^2}\right)^{1/2} \times \frac{1}{1+e^{q^0/T}}\operatorname{Im}\mathbf{W}^F(q) \tag{13}$$

for massive dielectrons. As a result, we have

$$\frac{dR}{d^4q} = \frac{2\alpha}{3\pi q^2}\left(1+\frac{2m_l^2}{q^2}\right)\left(1-\frac{4m_l^2}{q^2}\right)^{1/2}\left(q^0\frac{dN^*}{d^3q}\right), \tag{14}$$

which ties the dielectron rate to the *virtual* photon rate N^* for spacelike momenta. In the preceding expression, the correlation function $\mathbf{W}(q)$ is the same as in Sec. II but now evaluated at $q^2 < 0$. Therefore, the spectral-function approach used for the rates in the hadronic phase naturally contains the rates for photons and dileptons. The resulting dilepton rates, when the additional two-pion piece $\mathbf{W}_{\pi\pi}$ is included, can be found in Ref. [5] and are briefly discussed later.

The recent photon measurement reported by PHENIX is actually extracted from low-mass dielectron data below the two-pion threshold, to avoid the large background from hadronic decays. To extract the photon rates, the PHENIX collaboration makes use of the following relation between photon and dilepton production:

$$\frac{dR}{d^4q} = \frac{2\alpha}{3\pi q^2}\left(1+\frac{2m_l^2}{q^2}\right)\left(1-\frac{4m_l^2}{q^2}\right)^{1/2}\mathcal{S}\left(q^0\frac{dN}{d^3q}\right), \tag{15}$$

where $\mathcal{S}$ is a process-dependent factor. This process-dependent factor goes to 1 for $q^2 \to 0$. For π_0 and η decays (which is the dominant hadronic background), $\mathcal{S} \to 0$ when $M \geqslant M_h$ (the mass of the hadron). By cutting out invariant masses less than the π and η mass, the background from hadronic decays is largely suppressed.

The assumption made in the PHENIX experiment is that $\mathcal{S} \approx 1$ when $M \ll q_T$. The high-q_T, low-mass electron pairs are then taken to the photon point via Eq. (15). Because our spectral-function approach has direct access to both photons and low-mass dileptons, we can easily determine (in a model-independent way) the $\mathcal{S}$ factor for hadronic production processes.

In Fig. 6, we plot (in arbitrary units) the virtual photon rate ($q^0dN^*/d^3q \equiv \mathcal{S}q^0dN/d^3q$), where q^0dN^*/d^3q is the rate of virtual photon production Eq. (14) The left-hand panel includes only $\mathbf{W}_\pi$ while the right-hand panel includes $\mathbf{W}_\pi + \mathbf{W}_{\pi\pi}$. We fixed the three-momentum to $\vec{q} = 0.25$, 0.5, 1, and 3 GeV. If our process-dependent factor $\mathcal{S}$ was indeed equal to 1, we would not see any mass dependence in our plotted q^0dN^*/d^3q. This is not the case, however. For our leading-order ($\mathbf{W}_\pi$) rates at $\vec{q} \geqslant 0.5$, the factor $\mathcal{S}$ varies by a few percent up to a mass of 300 MeV. If this was the dominant thermal process, then the photon extrapolation made by PHENIX would be satisfactory. However, when the more complicated production mechanisms contained in $\mathbf{W}_{\pi\pi}$ are included, the $\mathcal{S}$ factor can change by as much as 30% at $M = 300$ MeV when $\vec{q} = 1$ GeV. Because PHENIX fits the low-mass electrons in the $100 \leqslant M \leqslant 300$ MeV region, we can confidently say that our $\mathcal{S}$ factor gives a discrepancy of $\approx$15%. This leads to a fairly large unconstrained systematic error in the PHENIX extrapolation procedure. We stress the fact that this error is unconstrained because the $\mathcal{S}$ factor could in principal be very different in the QGP, where the production mechanisms may be much different.

Let us conclude this section with a quick discussion on the dilepton rates in the QGP phase. These rates are used in our analysis of the PHENIX data in Sec. III B. Naively, one would expect the leading-order Born contribution, $q\bar{q} \to \gamma^*$, to dominate the dilepton mass spectrum. This breaks down at low mass because of phase-space constraints. For $M \lesssim m_{\text{th}}$, the next-to-leading-order contribution starts to take over. All of the same considerations for photons must be taken into account for dileptons including the HTL resummation, the summation of ladder diagrams, and the inclusion of the LPM effect. This was worked out in full for dileptons in Refs. [20]. For applications,we use the parametrization of this result from Refs. [21,22]. These rates are applicable in the kinematic regions where $q_0 > M$, $q_0 > T$, and $M^2 \sim g_s^2T^2$. The PHENIX acceptance can fall outside of these regions, so we caution the reader to this additional systematic uncertainty that comes about when comparing to experiment. To the LPM rates one must also add the $2 \to 2$ process worked out in Ref. [23], which was computed in the approximation $M \lesssim T$ and $q_0 \gg T$.

III. SPECTRA IN ULTRARELATIVISTIC HEAVY-ION COLLISIONS

Before a direct comparison with data can be made, the photon emission rates of the QGP and hadronic phases must be integrated over the space-time evolution of the collision. The collision region is modeled using a relativistic hydrodynamic simulation tuned to reproduce hadronic observables. In this section, we discuss the specifics of the model, including the initial conditions and equation of state (EOS) but leave the technical details to the literature.

The required initial conditions for the hydrodynamic evolution are the entropy density, $s(x, y)$, and baryon density, $n_B(x, y)$, in the transverse plane for a given impact parameter[3] (b) and initial proper time (τ_0). The entropy and baryon density are proportional to the number of wounded nucleons (participants), which is set by a Glauber model. More precisely, the initial condition is

$$\begin{aligned} s(\mathbf{r}, b) &= \frac{C_s}{\tau_0}\frac{dN_{WN}}{d^2\mathbf{r}}(\mathbf{r}; b), \\ n_B(\mathbf{r}, b) &= \frac{C_B}{\tau_0}\frac{dN_{WN}}{d^2\mathbf{r}}(\mathbf{r}; b), \end{aligned} \tag{16}$$

---

[3] In the present work, we actually do not perform off-central calculations. Instead the simulations are performed in 1+1D, where the system size is fixed to have the same number or participants. The resulting yields agree on the 10% level and are therefore within the overall uncertainty in our hydrodynamic model.

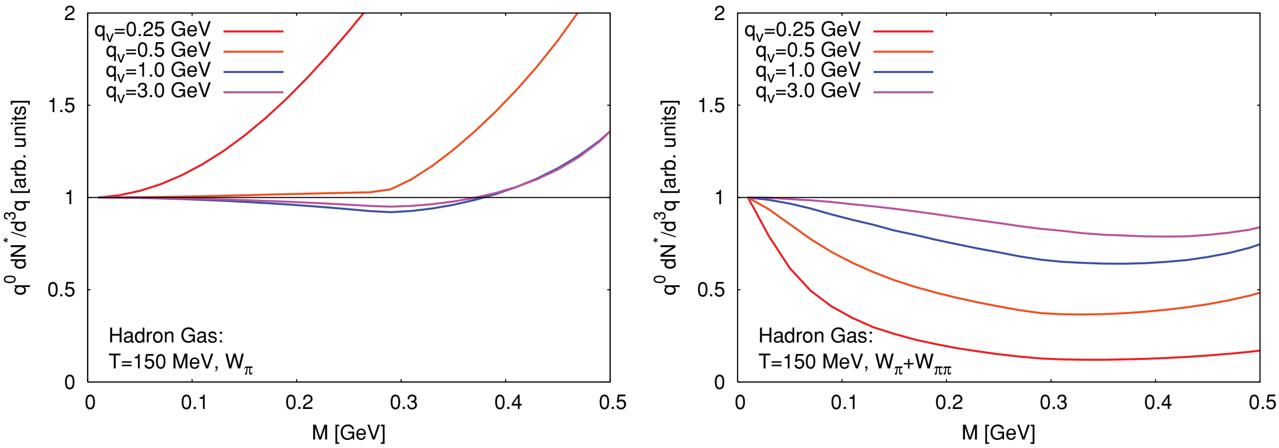

FIG. 6. (Color online) Rate of virtual photons (arbitrary units) from the spectral-function approach, including (left) $\mathbf{W}_\pi$ and (right) $\mathbf{W}_\pi + \mathbf{W}_{\pi\pi}$.

where $C_s \equiv 1/N_{\text{part}} dS/dy$ ($C_B \equiv 1/N_{\text{part}} dn_B/dy$) is the entropy (net baryon) density per unit rapidity per participant and is set to reproduce the charged-particle multiplicity and net proton number, respectively. Once the initial conditions are set, the hydrodynamic evolution equations are solved. The resulting evolution yields the energy density and flow velocity as a function of proper time τ and transverse coordinate. The energy density can then be converted to a temperature using the given EOS. The rates are then integrated over the space-time volume following the same procedure as in Refs. [24,25].

Table I shows the parameters used for the SPS, RHIC, and LHC. For RHIC, we used two different evolution models (labeled RHIC 1 and RHIC 2) to study the effects of the space-time evolution. We discuss the specific evolution models as they become relevant in the following sections.

We should stress that we make no attempt to perform global fits to the data. There are still a number of uncertainties present in the hydrodynamic model that would affect the resulting photon yields. The approach taken in this work is to choose parameters for our evolution model that yield a reasonable description of bulk observables such as the total multiplicity, p_T spectra, and elliptic flow. An example of one uncertainty is the shear viscosity, which when included would require us to retune the initial conditions to achieve the correct final-state multiplicities (as shown in Ref. [26]). In addition, viscous corrections also modify the underlying photon and dilepton rates [27,28]. These considerations are all beyond the scope of this work and should be thought of as part of the overall uncertainty in our evolution model.

TABLE I. Hydrodynamic parameters for SPS, RHIC, and LHC.

Parameter	SPS	RHIC 1	RHIC 2	LHC
$\sqrt{s_{NN}}$ (A GeV)	17.3	200	200	5500
A	208	197	197	208
$\sigma_{NN}^{\text{in.}}$ (mb)	33	40	40	60
C_s	8.06	20.8	20.8	42
C_B	0.191	0.	0.	0.
EOS	BM	Lat	Lat	Lat
Centrality	0%–10%	0%–20%	0%–20%	0%–20%
b (fm)	3	4.5	4.5	4.8
N_{part}	340	269	269	293
τ_0 (fm/c)	1	1	0.5	0.5
$T(\mathbf{r}_\perp = 0, \tau_0)$ (MeV)	245	336	398	501
$T_{\text{freezeout}}$ (MeV)	120	140	160	140

A. SPS: Photons at WA98

The WA98 collaboration measured direct photons from Pb+Pb collisions at $\sqrt{s} = 158$ GeV/nucleon using the statistical subtraction method in Refs. [29,30]. In this case, upper limits could be obtained for photon momentum in the range $0.5 \leqslant q_\perp \leqslant 1.5$ and data points obtained above 1.5 GeV. In addition, the yield of direct photons was also measured in Ref. [31] using direct photon interferometry. The most probable yield is found by assuming a source size of 6 fm, and a lower limit is obtained by assuming a vanishing R_{out}. The data are summarized in the left-hand plot of Fig. 7.

Figure 7 shows our predicted yields using the SPS hydrodynamic evolution from Table I. In this case we used parameters identical to those in Ref. [32]. This work used a bag model EOS with a latent heat of 0.8 GeV/fm^3 and was able to reproduce the p_T spectra and elliptic flow at the SPS. Above 2 GeV, one must also include the prompt production, which we left out in this analysis. This additional contribution was discussed thoroughly in Ref. [8]. Our results are consistent with the upper limits that were obtained at intermediate momentum.

The right-hand panel figure of Fig. 7 is the same as the left but rescaled in q_T between 0 and 0.8 GeV. This figure shows the leading-order QGP along with the single-pion process $\mathbf{W}_\pi$ are almost an order of magnitude below the data. By including the additional $\mathbf{W}_{\pi\pi}$ component, our rates are now at the lower limit of the data. In addition, one may question how changes to the evolution might affect the results. It is very probable that one could find a different set of parameters that reproduces the hadronic data at the SPS while increasing the yields of direct photons. This type of global analysis is beyond the scope of

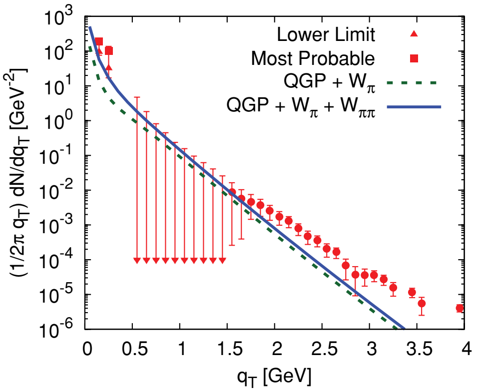

FIG. 7. (Color online) Photon spectra at the SPS: (left) data comparison for $0 \leqslant q_\perp$ (GeV) $\leqslant 4$ and (right) same as left but for $0 \leqslant q_\perp \leqslant 0.8$ GeV. See text for details.

this work. It is clear, however, that pion bremsstrahling as encoded in $\mathbf{W}_{\pi\pi}$ is a necessary component to understanding the direct photons at SPS.

We should stress that the role played by baryons is large at low momentum [33]. Although baryons were not included in this work, we can still estimate the enhancement by looking at other calculations. The work of Steele *et al.* [34,35] found that baryons, when treated to first order in nucleon density, can increase the rates relative to $\mathbf{W}_\pi$ by an order of magnitude at $q_T \approx 0.5$ GeV. Based on Fig. 2, we can estimate that the inclusion of nucleons could increase our overall rates (when the πN contribution is added to $\mathbf{W}_{\pi\pi}$) by a factor of about 2. This would comfortably keep us within the WA98 data.

B. RHIC: Photons at PHENIX

Let us now address the recent PHENIX measurements of photons. For Au + Au collisions at RHIC energies ($\sqrt{s} = 200$ GeV), we chose to use two different evolution models (called RHIC 1 and RHIC 2) to understand some of our systematic uncertainty stemming from the hydrodynamic evolution. In both cases, we use a lattice-themed EOS [36], which includes a rapid crossover followed by an interpolation into the hadronic resonance gas phase. Even though there is no true phase transition, we still must choose a value of T_c where we switch from QGP to hadronic production. Of course, this choice of T_c does not affect the hydrodynamic evolution, which is determined only by the sound speed. We fix this to $T_c = 190$ MeV, which is consistent with lattice calculations at almost physical quark masses [37,38].

The difference between RHIC 1 and RHIC 2 is the initial hydrodynamic starting time as well as the freezeout temperature. For RHIC 1, we have $\tau_0 = 1$ fm$/c$ and $T_{\text{freezeout}} = 140$ MeV. In the case of RHIC 2, we started the hydrodynamic evolution even earlier, at $\tau_0 = 0.5$ fm$/c$. In this case, to have reasonable agreement with bulk observables, one must use a higher freezeout temperature, $T_{\text{freezeout}} = 160$ MeV. The RHIC 1 parameter set is closer to the one used in Refs. [26,39], which found good agreement with the elliptic flow of hadrons. In the case of RHIC 2, we expect to have a larger contribution coming from the QGP phase and a smaller contribution from the hadronic phase. Note that we do not include any out-of-equilibrium contributions (other than the prompt contribution) before our initial starting time τ_0.

In Fig. 8 we show the hydrodynamically evolved photon emissivities using the evolution parameters of Table I for RHIC 1 (left) and RHIC 2 (right). The yields from the hadronic gas and QGP cross at $q_\perp \approx 1.5$ and 0.6 for RHIC 1 and RHIC 2, respectively. The earlier thermalization in the

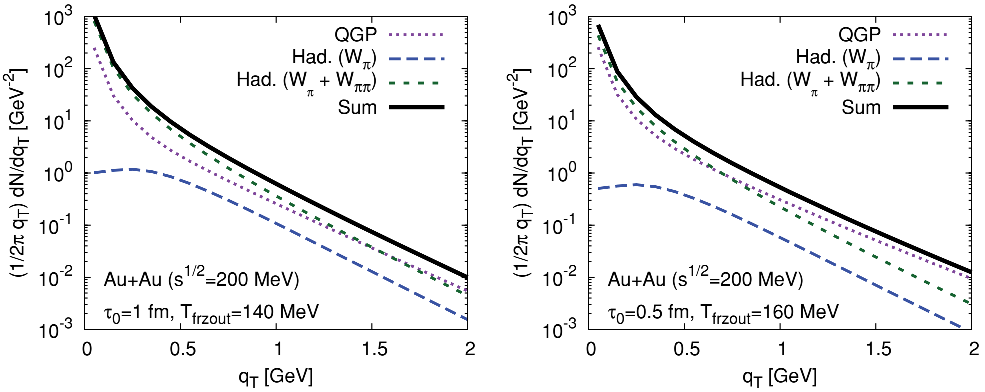

FIG. 8. (Color online) Photon spectra from hadronic sources vs the QGP at RHIC: evolution models (left) RHIC 1 and (right) RHIC 2 (see Table I).

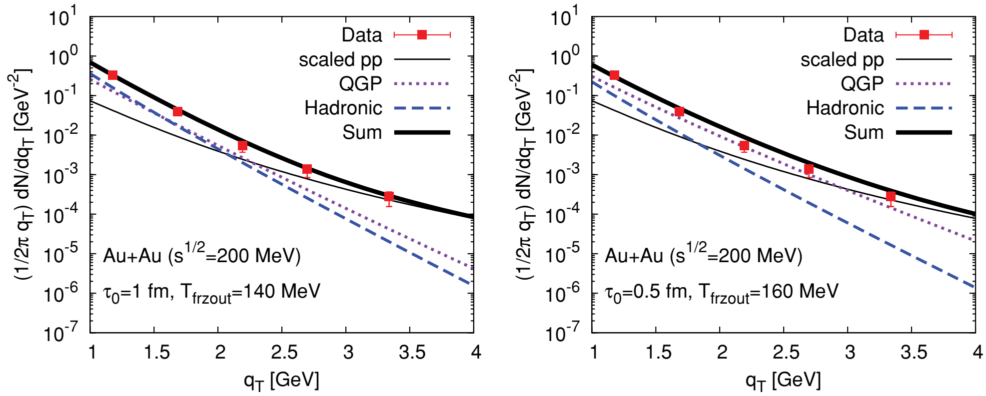

FIG. 9. (Color online) Photon spectra at RHIC compared to the recent PHENIX data: evolution sets (left) RHIC 1 and (right) RHIC 2 (see Table I).

RHIC 2 evolution gives a much larger QGP contribution at high momentum.

We now come to the recent measurement of direct photons by PHENIX [40]. We are now slightly hypocritical. In Sec. II C, we stressed that there is a large uncertainty in extrapolating the photon signal from low-mass dilepton data. We demonstrated for the hadronic gas used in this work that the discrepancy can be as large as ≈15%. Regardless, we plot our results for photon production on top of the PHENIX data, keeping in mind that there is at least a 15% uncertainty in their extraction.

Figure 9 shows the evolved photon rates versus the RHIC data for the two different hydrodynamic setups in Table I, (left) RHIC 1 and (right) is RHIC 2. We also included the prompt photon production, which is derived from a fit to the measured photons in *pp* collisions scaled by the number of binary collisions.

Our finding is that even though the relative contributions from the different phases are much different the sum remains about the same for the two different evolution models. In the case of RHIC 1, the relative QGP and hadronic contributions are about equal. For RHIC 2, the QGP has a larger contribution to the overall yield (which grows with increasing $q_\perp$). The differences in the two models are largest at high $q_\perp$, where the prompt production dominates. Taking into consideration all of the systematic uncertainties that we discussed throughout this work, it is impossible to discriminate between the two evolution models. This suggests that there may be a large ambiguity in using photons as an early time probe of the medium.

C. RHIC: Low-mass dileptons at PHENIX

We would now like to revisit our past analysis [41] of the measurement of dielectron pairs by PHENIX [42,43]. In our prior work, we used the leading-order Born contribution ($q\bar{q} \to \gamma^*$) as the only reaction present in the QGP phase. Although this is true at high mass, the naive perturbative expansion breaks down at low mass, which might explain the missing low-mass yield from theoretical models [44]. We therefore included, in addition to the Born contribution, the next-to-leading-order contribution. The rates used in this analysis were summarized at the end of Sec. II C. For the analysis of the low-mass dileptons, we chose to use the RHIC 2 evolution model. Even though this parameter set is for more central collisions ($b = 4.5$ fm), we make a direct comparison with the minimum bias data. In principal we could perform runs at various centralities and average accordingly to make a more direct comparison, but that approach is beyond the scope of this work.

In the left plot of Fig. 10 we show the individual contributions to the low-mass dielectron yield. New to this figure is the inclusion of the $\mathbf{W}_{\pi\pi}$ component in the hadronic phase. Even though this component added a lot of strength to the low-momentum photons, the effect is much less dramatic in the case of dileptons. There is a large enhancement in the dilepton rates at low mass *and* low q_T as demonstrated in Ref. [5]. By $M \sim 100$ MeV, almost all of the enhancement contained in $\mathbf{W}_{\pi\pi}$ is removed by the low-M_T cuts of the PHENIX acceptance. Therefore, to a very good approximation, our $\mathbf{W}_{\pi}$ makes up the entire hadronic yield at PHENIX after the acceptance cuts. Also shown in Fig. 10 is the QGP Born contribution. As we can see, this contribution diminishes at low mass owing to phase space. However, when we include the next-to-leading-order (NLO) corrections, the QGP yield starts to increase below $2M_{\rm th}$ and actually overtakes our hadronic contribution below $M \approx 500$ MeV. At high mass (above ≈1 GeV), the NLO rates are suppressed relative to the Born term because of the thermal quark mass.[4]

The right-hand plot of Fig. 10 shows the total yields, which include summing the cocktail provided by PHENIX along with our thermal hadronic and QGP yields. We showed the net yield using only the Born contribution (sum with Born only), which is essentially the result from our previous work [41]. We also show the yield using the full leading order in α_s result (sum with NLO QGP). The leading-order QGP explains the excess in the mass region $100 < M < 150$ MeV. About 50% of the thermal QGP production in this mass region is because of the one-loop Compton and annihilation processes. The other 50% required to explain the excess comes from the higher-loop

---

[4] One could reproduce the NLO rates above ≈1 GeV by simply using the Born rate with massive ($m \sim gT$) quarks.

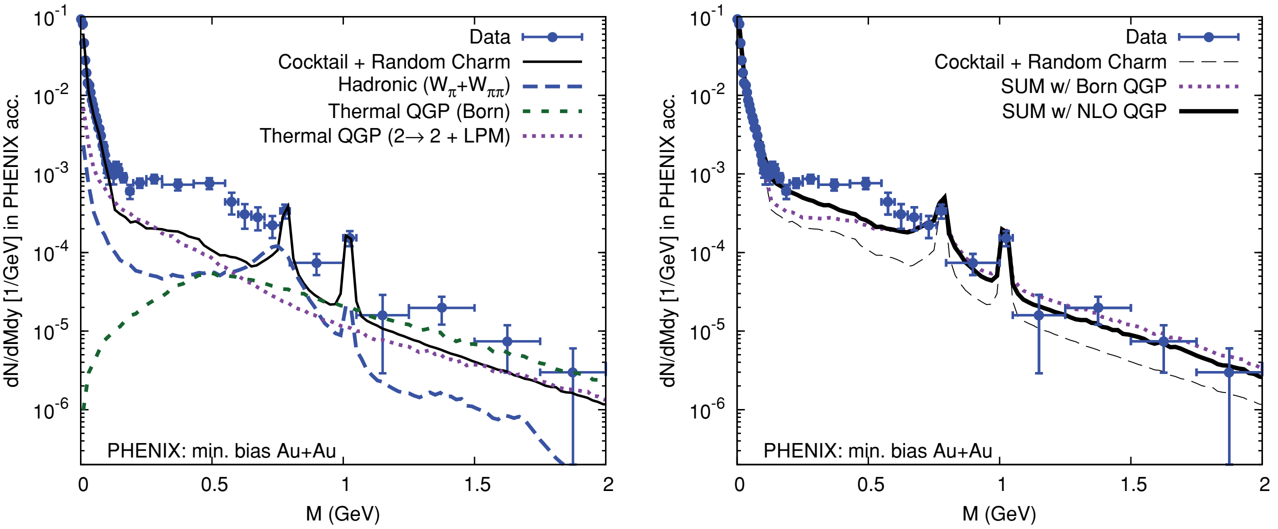

FIG. 10. (Color online) Dielectron spectra as measured by PHENIX: (left) various individual contributions to the thermal yield; (right) total yield using (1) the leading-order Born contribution and (2) the next-to-leading-order QGP contribution.

processes included in the ladder diagram resummation. The two-loop piece of this corresponds to the bremsstrahling diagrams. One should not be surprised that the QGP contribution overtakes the hadronic yield at low mass. It is already known that quark bremsstrahling dominates over π bremsstrahling in the $\vec{q}$-integrated rates [45,46]. In addition, the q_T spectrum of the π bremsstrahling falls much quicker than that of the quark bremsstrahlung, which only increases the relative yield of the quark to pion contribution when low-q_T cuts are applied. Larger transverse flow in the hadronic gas alleviates this picture by shuffling strength from low q_T to high q_T but it cannot compensate for the differences in the q_T spectrum.

Even though the addition of the full leading-order QGP rates does not explain the excess in the mass region $250 < M < 550$ MeV, it does help in adding some strength to the yield in this mass region. The mechanism behind the excess in the 250–550-MeV region is still unclear. What the authors find striking is the resemblance between the excess seen here and the excess observed in lower-energy C+C and Ca+Ca collisions, referred to as the "DLS puzzle." The resolution was related to a better theoretical understanding of bremsstrahling production in $p + n$ collisions and verified by looking at $p + p$ and $p + d$ control measurements [47]. In light of this, it might be useful to have a cocktail available that has been constrained by measured dileptons in $p + d$ or d + Au collisions at RHIC energies.

D. LHC: Predictions

In this final section, we would like to make some predictions for the photon production rate we expect for LHC conditions. It is very difficult to tune our hydrodynamic model without having any data on the net multiplicities. Instead we have set our initial condition to approximately yield the predicted multiplicity [48,49]. In going from RHIC to LHC, the inelastic nucleon-nucleon cross section, which enters into the wounded nucleon profiles, has increased from 40 to 60 mb. We also doubled the initial entropy density. Our final parameter set is summarized in Table I and is in qualitative agreement with the hydrodynamic models used in Refs. [50,51].

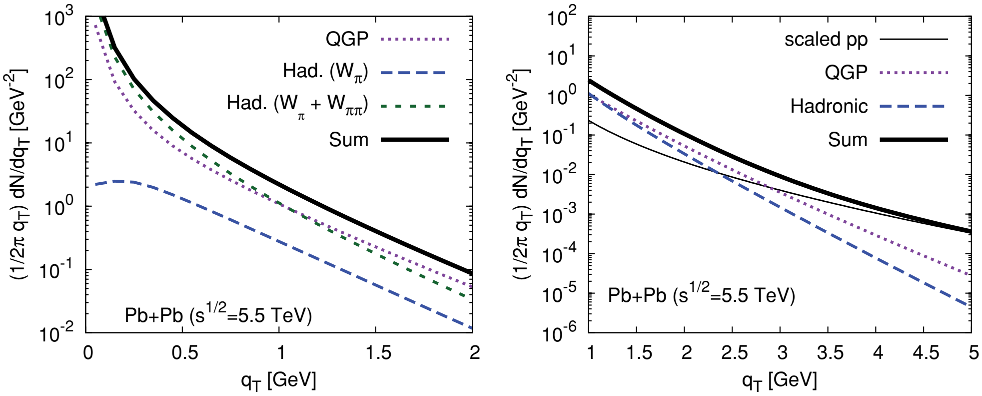

FIG. 11. (Color online) Prediction for photon yields from Pb+Pb collisions at $\sqrt{s} = 5.5$ TeV: (left) relative contribution from $\mathbf{W}_\pi$, $\mathbf{W}_{\pi\pi}$ and the QGP phase for $0 \leqslant q_T$ (GeV) $\leqslant 2$; (right) relative contributions from hadronic ($\mathbf{W}_\pi + \mathbf{W}_{\pi\pi}$), QGP, and prompt production for $1 \leqslant q_T \leqslant 5$ GeV.

In Fig. 11 we display our projected photon emissivities at LHC. The hadronic and QGP yields cross around $q_T \approx 1$ GeV with the hadronic gas dominating at low momentum. We also included predictions for the prompt photon production in $p + p$ at LHC energies [52] scaled to Pb + Pb collisions. The prompt production starts to dominate the yield above $q_T \approx$ 2.5–3.0 GeV, similar to what was found at RHIC.

IV. CONCLUSIONS

In this work, we provided an analysis of the photon emissivities over a large range of collision energies ranging from the SPS ($\sqrt{s} = 158$ GeV) to RHIC ($\sqrt{s} = 200$ GeV) and to predictions at the LHC ($\sqrt{s} = 1.5$ TeV). The analysis incorporates both hadronic and QGP rates integrated over an underlying hydrodynamic evolution tuned to bulk observables. In this section, we summarize the main conclusions of our work:

(i) We have extended the chiral-reduction approach to include terms to second order in pion density. The new addition of this work is inclusion of processes of the type $X \to \pi\pi\gamma$. The use of a spectral-function approach allows us to treat both dilepton and photon production on an equal footing and to incorporate broken chiral symmetry in a systematic fashion. We stress that our hadronic rates are parameter free and are completely constrained by τ decay, electroproduction, and Compton scattering data.

(ii) Using our hadronic rates, we tested the low-mass extrapolation used by PHENIX and found that we may expect a systematic error in their procedure of at least 15%.

(iii) We found that the pion bremsstrahling process, encoded in $\mathbf{W}_{\pi\pi}$, leads to a considerable photon enhancement in the low-energy region. These processes are a necessary ingredient in a quantitative understanding of the low-energy ($q_\perp \lesssim 500$ MeV) photon data, as demonstrated by the recent WA98 measurements (see Fig. 7).

(iv) The hadronic and LO QGP photon rates are able to adequately describe the RHIC data. We found that two different evolution models, which have different relative yields from the QGP and hadronic phases, are both able to describe the data.

(v) We readdressed the low-mass dilepton data from PHENIX. Our findings are (1) the $W_{\pi\pi}$ processes are completely removed by the acceptance cuts and (2) inclusion of the NLO dilepton rates from the QGP are able to account for the enhancement found in the $M = 100$–150 MeV region.

ACKNOWLEDGMENTS

K.D. would like to thank Stefan Bathe for useful discussions and Dmitri Peressounko for providing the SPS photon result from the HBT analysis. K.D. would also like to thank Werner Vogelsang for providing his prompt photon production calculations. We are also indebted to Axel Drees for stressing to us the role of the NLO corrections in the analysis of the PHENIX dielectron data. Finally, we are grateful to Ralph Rapp for his careful reading of our manuscript and for making many useful suggestions. K.D. is supported by US DOE Grant No. DE-AC02-98CH10886. The work of I.Z. was supported in part by US DOE Grants No. DE-FG02-88ER40388 and No. DE-FG03-97ER4014.

---

[1] M. Le Bellac, *Thermal Field Theory* (Cambridge University, Cambridge, UK, 1996).

[2] H. Yamagishi and I. Zahed, Ann. Phys. (NY) **247**, 292 (1996).

[3] J. V. Steele, H. Yamagishi, and I. Zahed, Phys. Lett. B **384**, 255 (1996).

[4] Z. Huang, Phys. Lett. B **361**, 131 (1995).

[5] K. Dusling, arXiv:0901.2027 [nucl-th].

[6] S. Chernyshev and I. Zahed, arXiv:hep-ph/9511271.

[7] V. L. Eletsky and B. L. Ioffe, Phys. Rev. D **51**, 2371 (1995).

[8] S. Turbide, R. Rapp, and C. Gale, Phys. Rev. C **69**, 014903 (2004).

[9] C. H. Lee, H. Yamagishi, and I. Zahed, Phys. Rev. C **58**, 2899 (1998).

[10] W. Liu and R. Rapp, Nucl. Phys. A **796**, 101 (2007).

[11] J. I. Kapusta, P. Lichard, and D. Seibert, Phys. Rev. D **44**, 2774 (1991); **47**, 4171(E) (1993).

[12] E. Braaten and R. D. Pisarski, Nucl. Phys. B **337**, 569 (1990).

[13] R. Baier, H. Nakkagawa, A. Niegawa, and K. Redlich, Z. Phys. C **53**, 433 (1992).

[14] P. Aurenche, F. Gelis, R. Kobes, and E. Petitgirard, Phys. Rev. D **54**, 5274 (1996).

[15] P. Aurenche, F. Gelis, R. Kobes, and E. Petitgirard, Z. Phys. C **75**, 315 (1997).

[16] P. Aurenche, F. Gelis, H. Zaraket, and R. Kobes, Phys. Rev. D **58**, 085003 (1998).

[17] P. Arnold, G. D. Moore, and L. G. Yaffe, J. High Energy Phys. 11 (2001) 057.

[18] P. Arnold, G. D. Moore, and L. G. Yaffe, J. High Energy Phys. 12 (2001) 009.

[19] P. Arnold, G. D. Moore, and L. G. Yaffe, J. High Energy Phys. 6 (2002) 030.

[20] P. Aurenche, F. Gelis, G. D. Moore, and H. Zaraket, J. High Energy Phys. 12 (2002) 006.

[21] S. V. Suryanarayana, Phys. Rev. C **76**, 044903 (2007).

[22] S. V. Suryanarayana, Phys. Rev. C **75**, 021902 (2007).

[23] M. H. Thoma and C. T. Traxler, Phys. Rev. D **56**, 198 (1997).

[24] K. Dusling, D. Teaney, and I. Zahed, Phys. Rev. C **75**, 024908 (2007).

[25] K. Dusling and I. Zahed, Phys. Rev. C **80**, 014902 (2009).

[26] M. Luzum and P. Romatschke, Phys. Rev. C **78**, 034915 (2008).

[27] K. Dusling and S. Lin, Nucl. Phys. A **809**, 246 (2008).

[28] K. Dusling, Nucl. Phys. A **839**, 70 (2010).

[29] M. M. Aggarwal *et al.* (WA98 Collaboration), Phys. Rev. Lett. **85**, 3595 (2000).

[30] M. M. Aggarwal *et al.* (WA98 Collaboration), arXiv:nucl-ex/0006007.

[31] M. M. Aggarwal *et al.* (WA98 Collaboration), Phys. Rev. Lett. **93**, 022301 (2004).

[32] D. Teaney, J. Lauret, and E. V. Shuryak, arXiv:nucl-th/0110037.

[33] R. Rapp and J. Wambach, Eur. Phys. J. A **6**, 415 (1999).

[34] J. V. Steele, H. Yamagishi, and I. Zahed, Phys. Rev. D **56**, 5605 (1997).

[35] J. V. Steele and I. Zahed, Phys. Rev. D **60**, 037502 (1999).

[36] M. Laine and Y. Schroder, Phys. Rev. D **73**, 085009 (2006).

[37] F. Karsch, arXiv:hep-ph/0701210.

[38] M. Cheng *et al.*, Phys. Rev. D **77**, 014511 (2008).

[39] K. Dusling, G. D. Moore, and D. Teaney, Phys. Rev. C **81**, 034907 (2010).

[40] A. Adare *et al.* (PHENIX Collaboration), Phys. Rev. Lett. **104**, 132301 (2010).

[41] K. Dusling and I. Zahed, Nucl. Phys. A **825**, 212 (2009).

[42] S. Afanasiev *et al.* (PHENIX Collaboration), arXiv:0706.3034 [nucl-ex].

[43] A. Toia (PHENIX Collaboration), arXiv:0711.2118 [nucl-ex].

[44] A. Drees, Nucl. Phys. A **830**, 435c (2009).

[45] J. Cleymans, V. V. Goloviznin, and K. Redlich, Z. Phys. C **59**, 495 (1993).

[46] V. V. Goloviznin and K. Redlich, Phys. Lett. B **319**, 520 (1993).

[47] W. A. Zajc, Nucl. Phys. A **830**, 3c (2009).

[48] D. Kharzeev, E. Levin, and M. Nardi, Nucl. Phys. A **747**, 609 (2005).

[49] J. L. Albacete, Phys. Rev. Lett. **99**, 262301 (2007).

[50] H. Niemi, K. J. Eskola, and P. V. Ruuskanen, Phys. Rev. C **79**, 024903 (2009).

[51] M. Luzum and P. Romatschke, Phys. Rev. Lett. **103**, 262302 (2009).

[52] L. E. Gordon and W. Vogelsang, Phys. Rev. D **48**, 3136 (1993).